Contents lists available at ScienceDirect

Earth and Planetary Science Letters

www.elsevier.com/locate/epsl



Physicochemical models of effusive rhyolitic eruptions constrained with InSAR and DEM data: A case study of the 2011-2012 Cordón Caulle eruption



Francisco Delgado ^{a,b,*}, Julia Kubanek ^{c,1}, Kyle Anderson ^d, Paul Lundgren ^e, Matthew Pritchard ^a

- ^a Department of Earth and Atmospheric Sciences, Cornell University, Ithaca, NY, USA
- ^b Université de Paris, Institut de Physique du Globe de Paris, CNRS, F-75005 Paris, France
- ^c Department of Earth and Planetary Sciences, McGill University, Montreal, Canada
- ^d California Volcano Observatory, U.S. Geological Survey, Menlo Park, CA, USA
- ^e Jet Propulsion Laboratory, California Institute of Technology, Pasadena, CA, USA

ARTICLE INFO

Article history: Received 18 February 2019 Received in revised form 25 July 2019 Accepted 29 July 2019 Available online 13 August 2019 Editor: R. Dasgupta

Keywords: Cordón Caulle InSAR rhyolitic eruptions TanDEM-X magma compressibility

ABSTRACT

The 9 month long 2011-2012 eruption of Cordón Caulle (Southern Andes, Chile) is the best instrumentally recorded rhyolitic eruption to date and the first time that the effusion of a rhyolitic flow has been observed in detail. We use Interferometric Synthetic Aperture Radar (InSAR), with time-lapse digital elevation models (DEMs) and numerical models to study the dynamics of coupled magma reservoir deflation and lava effusion. InSAR recorded 2.2-2.5 m of subsidence after the first three days of the eruption, which can be modeled using a spheroidal magma reservoir at a depth of ~5 km, ~20 km long, and with a pressure drop of 20-30 MPa. The source is elongated in the NW-SE direction and its large dimensions imply a large plumbing system active throughout the eruption and spanning neighboring volcanoes, with a slight change in the geometry halfway through the effusive phase. TanDEM-X and Pléiades DEMs record the extrusion of both the rhyolitic lava flow and the intrusion of a shallow laccolith around the eruptive vent after the third day of the eruption, with a total volume of $\sim 1.45 \text{ km}^3 \text{ DRE}$. The laccolith was emplaced during the first month of the eruption, during both the explosive and effusive stages of the eruption. Both the reservoir pressure drop and the extruded volume time series follow quasi-exponential trends, and can be explained by a model that couples the reservoir pressure decrease, time- and pressure-dependent variations in the magma properties inside of the reservoir, and conduit flow. This model predicts both the temporal evolution and amplitude of both time series during the effusive phase, and a magma compressibility of $\sim 10^{-10}$ Pa⁻¹, half the reported compressibility of the magma of the sub-Plinian explosive phase. Further, we estimate that the reservoir contained 1-3 wt.% dissolved H2O at the onset of lava effusion, with no exsolved CO2 and H2O in the reservoir throughout the effusive phase. This implies that the magma was significantly degassed after the explosive phase. The remaining volatiles in the magma after the explosive stage might have caused magma fragmentation, consistent with the hybrid explosive-effusive style observed during the waning of the eruption.

© 2019 Elsevier B.V. All rights reserved.

1. Introduction

One of the key challenges in volcanology is to forecast both the onset and end of effusive and explosive eruptions (Sparks, 2003; Sparks et al., 2012; Bonny and Wright, 2017), which has been

traditionally made by real-time ground monitoring data such as seismicity, SO₂ emissions and ground deformation. Satellite observations, including the constellation of Synthetic Aperture Radar (SAR) (e.g., TerraSAR/TanDEM-X, COSMO-SkyMED, Sentinel-1) and optical missions (e.g., Pléiades) have provided a wealth of ground deformation and topographic data respectively that can be used to gain insights into the processes that lead to eruptions (e.g., Reath et al., 2019). Unfortunately, their application to study time-lapse magma transport has been limited because the repeat periods of these SAR missions are currently at best one image every 1-6 days, usually longer than the duration of many eruptions. So far, the

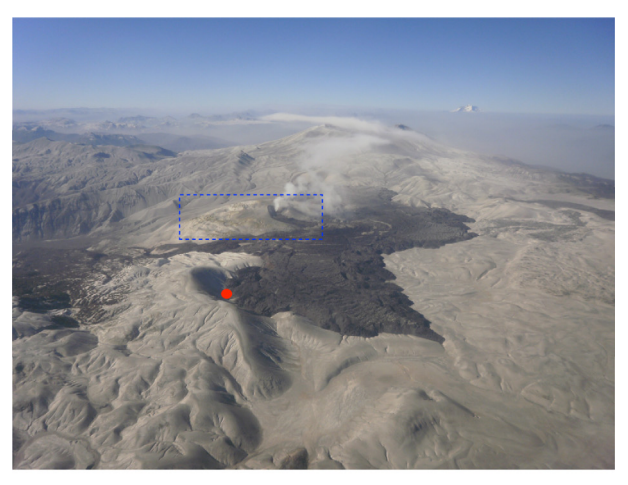
^{*} Corresponding author. E-mail address: delgado@ipgp.fr (F. Delgado).

¹ Now at European Space Research and Technology Centre, European Space Agency (ESA-ESTEC).

eruption with the best SAR temporal coverage is the 2018 eruption of Kilauea Volcano (Neal et al., 2018). InSAR data with short repeat periods (less than 12 days) have also provided key data to track time-dependent processes in effusive eruptions elsewhere (Xu et al., 2016; Dumont et al., 2018; Smittarello et al., 2019).

Co-eruptive geodetic data that record magma reservoir deflation are traditionally inverted for kinematic models that provide key information on the source location, shape and volume/pressure change (e.g., McTigue, 1987; Yang et al., 1988). Unfortunately, these models lack predictive capabilities because they do not consider physical processes in the magma reservoirs. We can overcome these limitations by using models that couple magma flow in a conduit and reservoir pressurization (e.g., Stasiuk et al., 1993; Huppert and Woods, 2002; Mastin et al., 2008; Anderson and Segall, 2011; Segall, 2013). These models show that the temporal evolution of extruded volume and the ground deformation can follow functions of the form $f(t)=f_e(1-e^{-t/\tau})$ with f_e and τ constants that are a function of the plumbing system geometry and magma properties. Indeed, ground deformation and the lava extruded volume in many basaltic (e.g., Stasiuk et al., 1993; Hreinsdottir et al., 2014; Gudmundsson et al., 2016; Coppola et al., 2017a; Kubanek et al., 2017) and silicic (e.g., Schilling et al., 2008; Pallister et al., 2013; Coppola et al., 2017b) effusive eruptions follow trends that resemble either logarithmic or exponential trends (hereafter quasiexponential). These simple exponential models have been useful to predict the end of several effusive eruptions (e.g., Gudmundsson et al., 2016; Coppola et al., 2017a; Bonny and Wright, 2017). The kinematic and magma flow models can be combined into physicochemical models (Anderson and Segall, 2011) based on solutions to coupled equations between magma chamber deflation, conduit flow, magma physical properties and observables including extrusion and geodetic (InSAR, GPS, tilt) data. Unfortunately it is very rare to have an accurate time series of extruded volume because they rely on expensive airborne methods (e.g., Pallister et al., 2013; Schilling et al., 2008). Nevertheless, when both topographic and geodetic data are available, it is possible to calculate the magma compressibility, which controls both the eruption duration and extruded volume (Huppert and Woods, 2002), and can explain discrepancies between the source volume change and extruded volume (Rivalta and Segall, 2008). These models also allow us to separate the source volume from the source overpressure, an advantage over kinematic models that do not allow for calculation of these parameters independent from each other (McTigue, 1987; Anderson and Segall, 2013). The use of time-lapse InSAR and satellite-derived DEMs facilitates development and utilization of more realistic and time-dependent models required to improve eruption forecasting and a better understanding of volcanic eruptions.

In this study we use both InSAR ground deformation and DEM data to understand the dynamics and evolution of the effusive phase of the 2011-2012 Cordón Caulle (CC) rhyolitic eruption (VEI 4-5). This eruption is a unique event because it is the best instrumentally recorded rhyolitic eruption (Castro et al., 2013, 2016; Schipper et al., 2013; Jay et al., 2014; Wendt et al., 2017), and one of the few effusive eruptions where both co-eruptive satellite geodetic and topographic time-lapse data were recorded. This makes CC one of the few volcanoes where the data sets required by a time-dependent eruption model are available, like Mount St. Helens (Anderson and Segall, 2013). The 2011-2012 eruption of Cordón Caulle lasted ~9 months, between June 4, 2011 until March 2012, and was the first eruption of the volcano since the VEI 4 1960 eruption (Lara et al., 2004). The climactic phase of the eruption lasted ~27 hours and ejected a ~9-12 km high eruptive column, with a VEI of 4 (Bonadonna et al., 2015). The eruption style shifted from purely explosive to hybrid explosive-effusive on June 15, with the extrusion of a rhyolitic lava flow (Fig. 1) punctu-



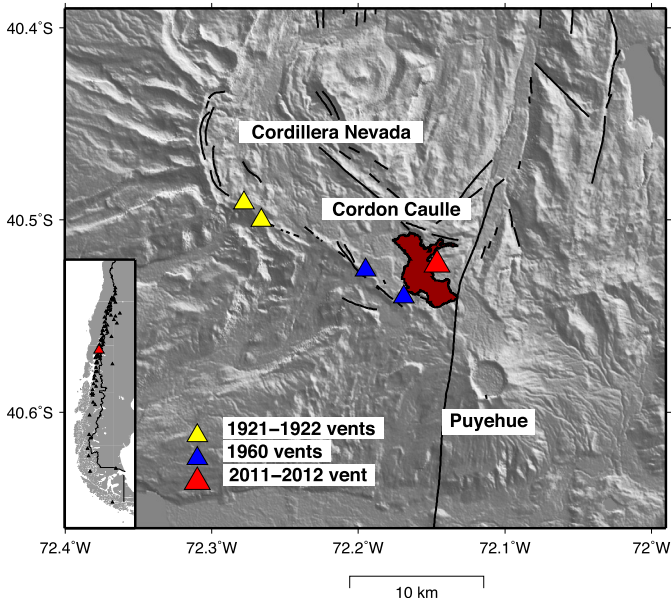


Fig. 1. Top. Airborne photograph of the 2011-2012 lava flow in March 2012 (courtesy of Daniel Bertin). The area inside the blue dashed box was uplifted 250 m during the first month of the eruption by the intrusion of a shallow laccolith (Figs. 3, 4). The red circle shows the location where visual observations of the lava flow were carried out on January 2017. Bottom. Cordón Caulle location map with SRTM shaded topography, eruptive vents (color triangles), the 2011-2012 lava flow (brown outline) and faults (black lines). All the eruptive vents are located in the NW-SE direction faults that bound the graben structure that makes up Cordón Caulle. The inset shows the location within South America, where the red triangle is Cordón Caulle. (For interpretation of the colors in the figure(s), the reader is referred to the web version of this article.)

ated by mixed ash-gas jets with Vulcanian blasts (Schipper et al., 2013; Castro et al., 2014). The lava time averaged discharge rate (TADR) decreased exponentially from the onset of extrusion until a second pulse of lava effusion between October-November 2011 and March 2012 (Coppola et al., 2017b). A shallow laccolith with a volume of \sim 0.8 km³ was emplaced at depths of 0.2-0.4 km during the first month of the eruption, (Castro et al., 2016). The total extruded magma has a bulk volume of $\sim 1.2~{\rm km^3}$ for the lava flow and the shallow laccolith (Castro et al., 2016), and of \sim 1.22 km³ for the tephra erupted between June 4-7, 2011 (Pistolesi et al., 2015). The erupted magma has a rhyolitic composition (lava 71-72% SiO₂) that overlaps that of the 1960 and 1921-1922 eruptions (Castro et al., 2013; Jay et al., 2014), and was stored at depths between 2.5 and 6 km (Castro et al., 2013; Jay et al., 2014; Wendt et al., 2017). InSAR data acquired during the first three days of the eruption (June 4-7) shows that two magma reservoirs located beneath Cordillera Nevada caldera (CNc) and Puyehue volcano (Pv) (Fig. 2)

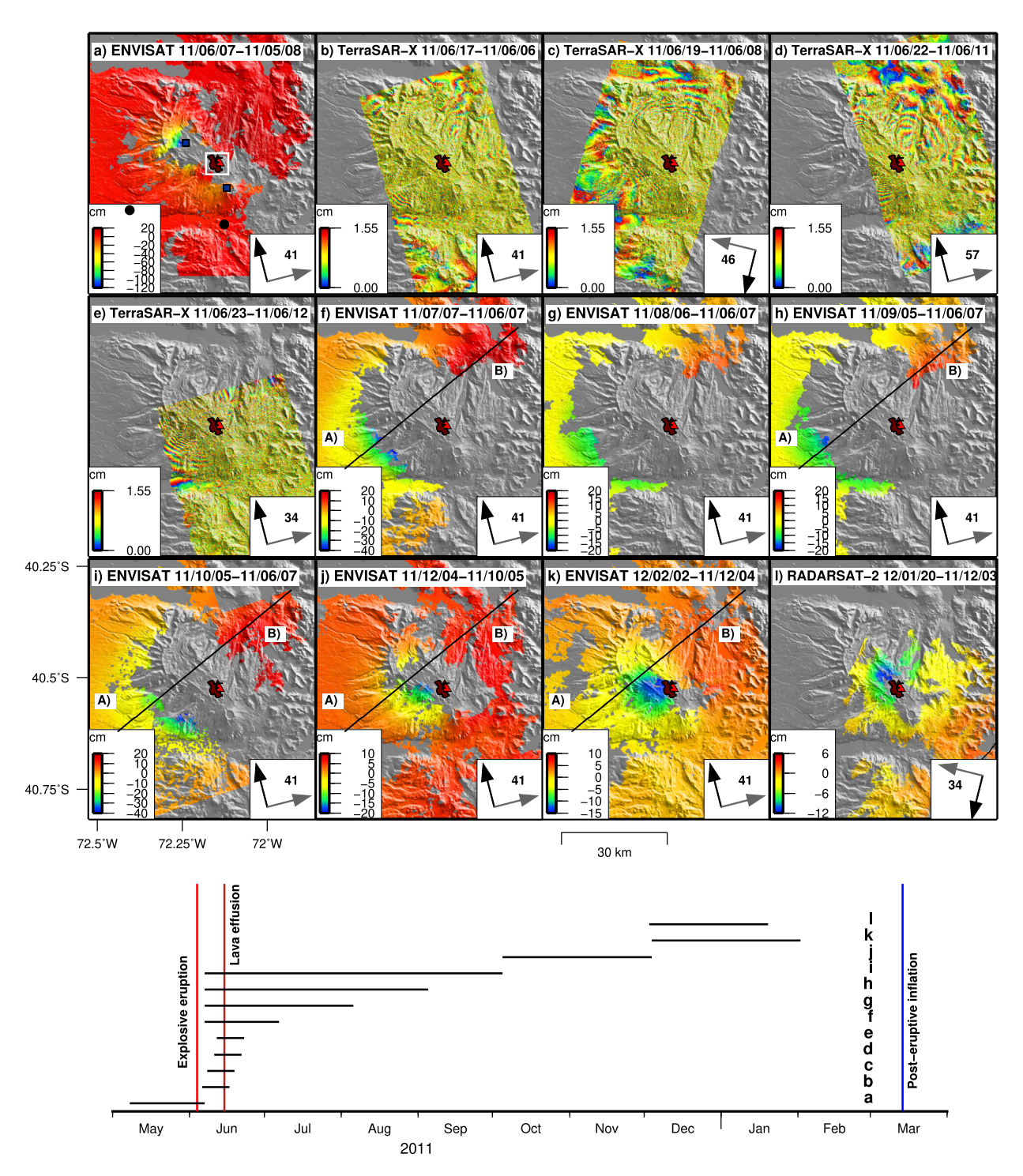


Fig. 2. Top. Co-eruptive InSAR data (legend year/month/day). Interferograms cover the first three eruption days (a) with two deflating sources (blue squares, Jay et al., 2014) and the rest of the eruption. Interferograms b-e are shown wrapped because the poor data coherence hampers reliable phase unwrapping across the whole scene. The black lines and the letters A and B in f, h-k show the location of the profiles of deformation in Fig. S6. The red triangle and the brown outline are the 2011-2012 eruptive vent and lava flow. The black arrow, grey arrow and number inside of the right white box in each interferogram are the satellite heading, horizontal line-of-sight vector and look angle, respectively. The dashed white box and the black circles in a) show the location of the TanDEM-X data in Fig. 4, and the location of the two GPS stations that recorded co-eruptive subsidence (Wendt et al., 2017), respectively. Bottom. The horizontal black lines show the time span of each interferogram with respect to the eruption timing (vertical lines). The letters show the time span of each interferogram.

deflated and produced more than 1 m of subsidence, whereas a single reservoir located beneath Cordón Caulle deflated with a quasi-exponential trend during the rest of the eruption (Jay et al., 2014; Wendt et al., 2017).

Here, we expand the available InSAR ENVISAT data with new RADARSAT-2 and TerraSAR-X interferograms, which are modeled with a prolate spheroidal source model and record a slight change in the deformation source halfway through the effusive phase. We then present volumes of the lava flow and shallow laccolith calculated from TanDEM-X DEMs starting on day three of the eruption. Finally, we combine the geodetic and topographic data sets in a physicochemical eruption model that incorporates time dependent magma properties to predict the magma volatile budget and compressibility and the eruption evolution during the effusive stage. We also correct an error in an analytical model for an effusive eruption (Segall, 2013, Supplementary material).

2. Data sets

InSAR and DEM data processing are described in detail in section 1 of the supplementary material (Figs. S1-S4).

2.1. InSAR and GPS

We use 16 ENVISAT IS6 interferograms processed by Jay et al. (2014) (also previously analyzed by Wendt et al. (2017) and Euillades et al. (2017)), and include five new TerraSAR-X (TSX) and RADARSAT-2 interferograms (Fig. 2). All of the interferograms record the time-lapse co-eruptive subsidence rather than bracketing the whole eruption, with variable amplitudes of \sim 5-20 cm, but interferograms with useful coherence in the summit area were only recorded during the waning of the eruption between December 2011 and March 2012. In addition to InSAR deformation data, we also analyze radar amplitude images (Figs. 3 and S4), allowing to track changes in the eruptive vent during the explosive-effusive transition, similar to previous studies (Castro et al., 2016). We do not use GPS data from two stations located ~15-25 km away from the eruptive vent (Wendt et al., 2017) because they were located too far from the volcano.

2.2. TanDEM-X and Pléiades topographic data

The lava flow volume was calculated with a set of six Coregistered Slant-range Single-look Complex (CoSSC) TanDEM-X (TDX) bistatic images (Fig. 4). These CoSSC were processed with a modified version of the Delft Object-oriented Radar Interferometric Software (DORIS) (Kubanek et al., 2017) to generate six DEMs. These DEMs were then subtracted to yield differential DEMs (hereafter dDEM). Additional elevation changes were calculated subtracting the global TanDEM-X DEM from the Shuttle Radar Topographic Mission (SRTM) DEM and a pre-eruptive CoSSC TDX DEM to a post-eruptive Pléiades DEM. Topographic changes in the lava flow have magnitudes up to 150 m, but east of the eruptive vent they have amplitudes up to 250 m, produced by the emplacement of a shallow laccolith during the eruption (Castro et al., 2016). The latter signal is absent in the pre-eruptive dDEM (Fig. 4a), thus it can be discarded as a SRTM error. For our purposes we consider the shallow laccolith as magma that was going to be erupted but was instead emplaced at depths < 0.5 km below the surface. For the bulk to dense rock equivalent (DRE) calculation we use a porosity of 10% (Schipper et al., 2015; Anderson and Segall, 2013) for both the lava flow and the shallow laccolith (section S1.2.4). The DRE TADR is then calculated by dividing the dDEM volume change by its time span (Fig. 5). The 2011-2012 DRE TADR is one

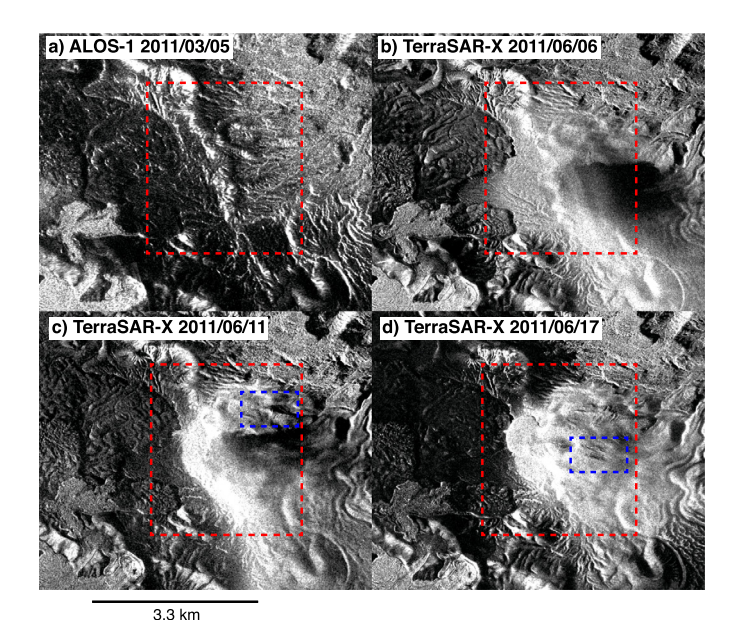


Fig. 3. Selected radar amplitude images of the eruptive vent and lava flow from ascending orbits of the ALOS (a) and TSX (b-d) satellites. The full catalog of amplitude images is shown in Fig. S4. These amplitude images cover the pre-eruptive (a), explosive (b-c), and hybrid explosive-effusive (d) phases. The red and blue boxes highlight the area where the shallow laccolith was emplaced and syn-eruptive deformation structures that were active at different times, respectively. The bulging produced by the shallow laccolith intrusion is shown in the red box in b-d, which implies that the laccolith started to be emplaced during the explosive stage (June 04-15, 2011).

of the largest that has been recorded for silica-rich effusive eruptions (Bertin et al., 2015; Pallister et al., 2013): up to 150 m³/s during the first 2.5 months of the eruption (Fig. 5) and decreasing quasi-exponentially until the end of the eruption. The total lava flow and laccolith DRE volume is 1.45 km³ for the TanDEM-X data and 1.38 km³ for the Pléiades data and were not separated due to the lack of a clear boundary between them. Because amplitude images show that part of the laccolith was emplaced during the explosive stage (Figs. 3, S4), this volume must be removed before any further modeling. The combined volume of the laccolith intruded during the effusive phase and the lava flow is estimated with an exponential fit to the time series of extruded volume, and then the predicted volume during the explosive phase is removed. This results in a total DRE volume of $\sim 1.21 \text{ km}^3$ during the effusive phase (Fig. 5, section S3).

3. Effusive phase models

3.1. Interferogram inversion

We use the 6 most coherent ENVISAT ascending interferograms and the TerraSAR-X descending interferograms for the source model inversion (Table S1). The interferograms were downsampled with a model-resolution algorithm (Lohman and Simons, 2005) using a horizontal sill at a depth of 4 km. This sill model is only used to increase the density of downsampled points in areas with ground deformation, not to invert the source geometry responsible for the ground deformation signal. The resulting downsampled interferograms were inverted using the neighborhood algorithm (Sambridge, 1999), a nonlinear inversion method that iteratively searches for the best fit model parameters. We separately invert for three source geometries: a pressurized sphere (McTigue, 1987). a horizontal pressurized prolate spheroid (Yang et al., 1988) and a compound dislocation model (CDM) (Nikkhoo et al., 2016).

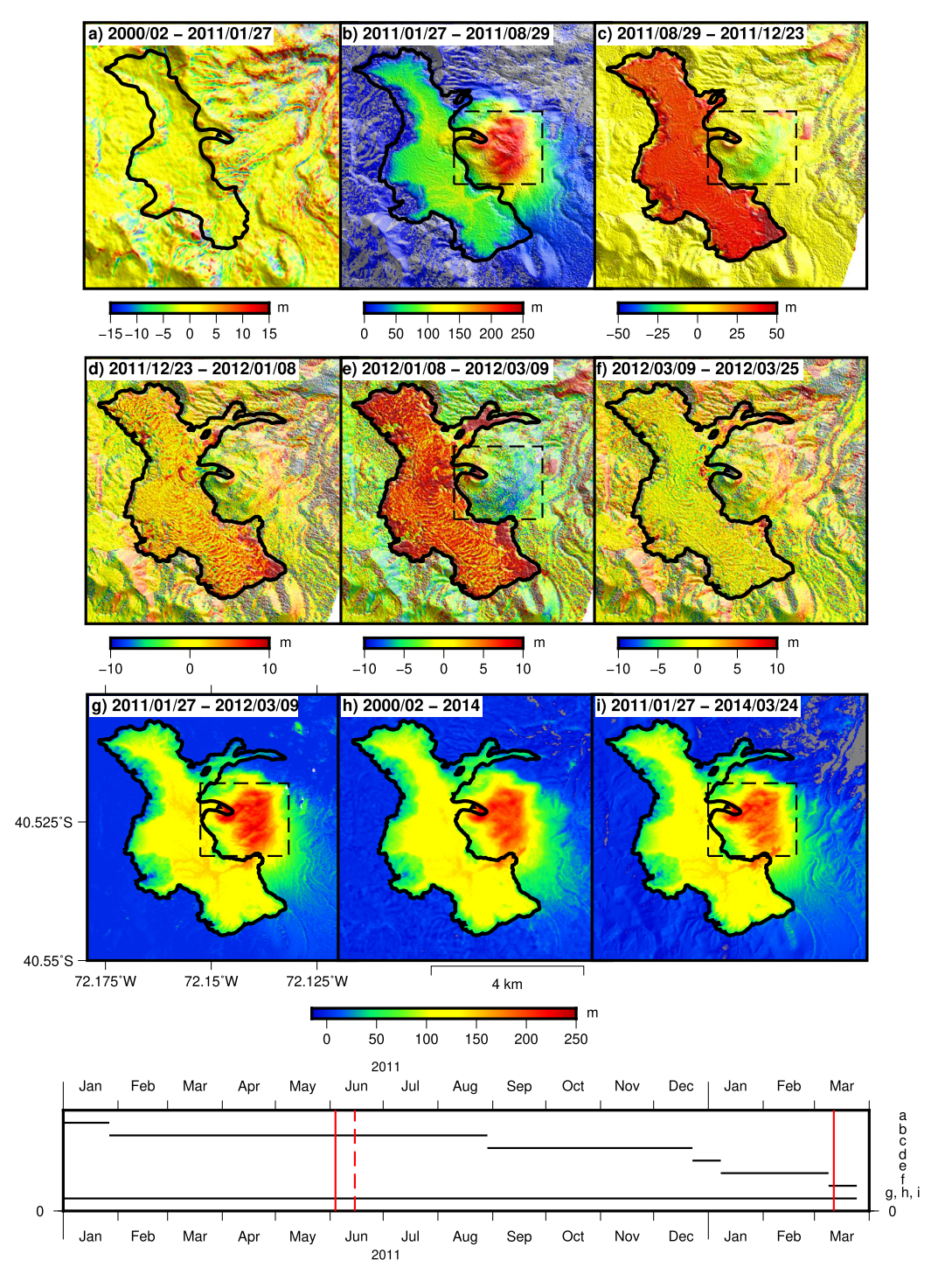


Fig. 4. Differential DEMs (dDEM) of the rhyolitic lava flow. All of these dDEMs are the differences between two TDX DEMs except a) which is the difference between SRTM and a pre-eruptive TDX COSSC DEM, h) which is the difference between the 12 m TanDEM-X DEM and the SRTM DEM, and i) which is the difference between a post-eruptive Pléiades DEM and a pre-eruptive TanDEM-X DEM. The topographic changes are produced by the extrusion of the lava flow (Bertin et al., 2015, outline is the black line) and by the intrusion of a shallow laccolith with a maximum of topographic change of ~250 m, and subsequent subsidence (dashed black line). The bottom panel shows the time span of the dDEM. The vertical red lines are the start and end of the eruption. The vertical dashed red line is the onset of lava effusion. The dDEM in g) - i) show the total co-eruptive topographic change and the difference in elevation in the area of the shallow laccolith between g and i suggests a post-emplacement mechanism.

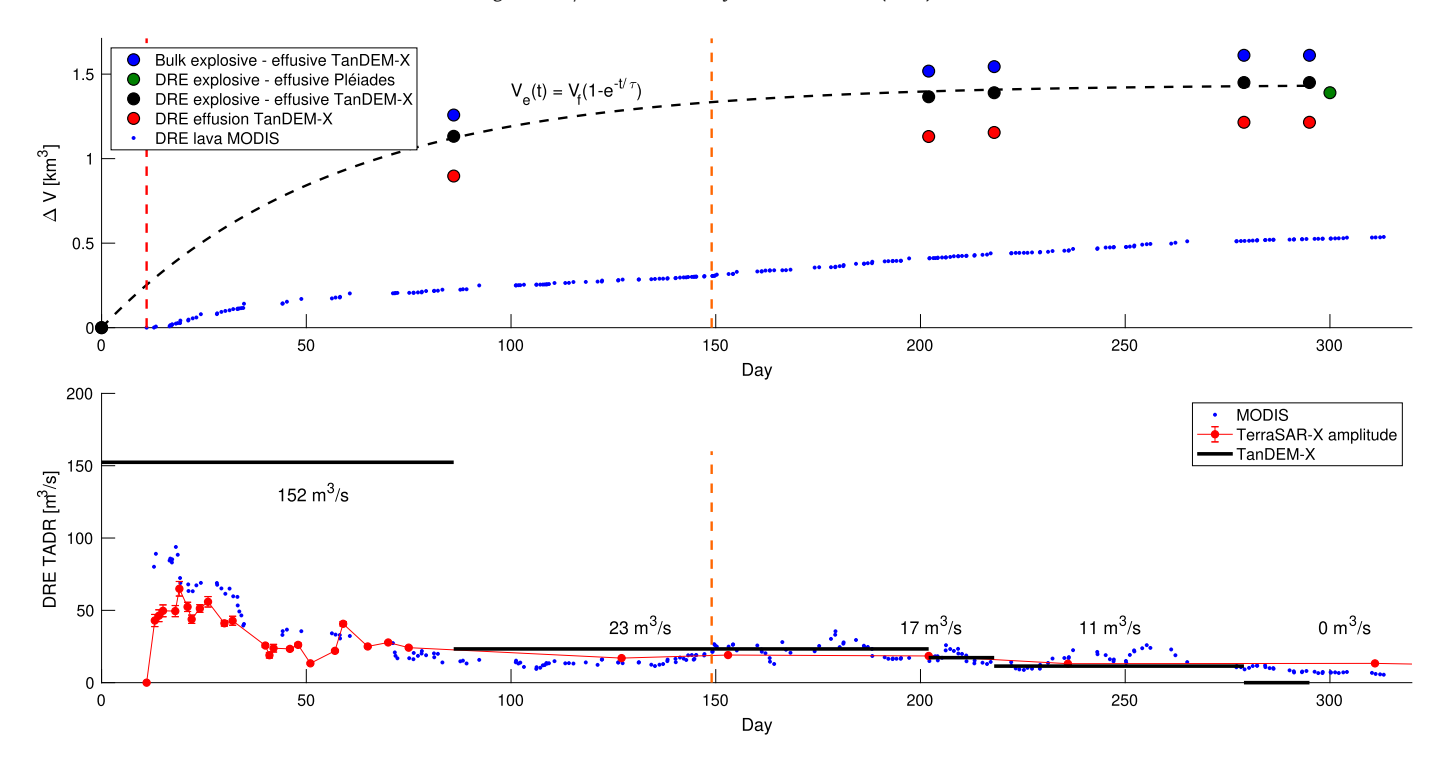


Fig. 5. Top. Time series of extruded lava and shallow laccolith intrusion DRE volume. The time series are from TanDEM-X (blue bulk volume, black DRE volume and red DRE volume during the effusive phase), Pléiades (green DRE volume) and MODIS data (Coppola et al., 2017b) (small blue dots). The black dashed line is the best fit for a function of the form $V_e = V_f (1 - e^{-t/\tau})$ with $V_f = 1.27$ km³ and $\tau = 51$ days. Bottom. TADR from TanDEM-X, optical and radar amplitude imagery planimetry (Bertin et al., 2015), and MODIS imagery (Coppola et al., 2017b). The vertical dashed orange line shows the onset of the second pulse of lava extrusion (Coppola et al., 2017b). The numbers on top of the horizontal black lines are the TanDEM-X TADR. The volume changes from the MODIS and planimetric data do not include the shallow laccolith (Coppola et al., 2017b).

3.2. Kinematic model

We seek the best source model that can model the whole ensemble of interferograms. Inversions of the ENVISAT and TSX interferograms with a sphere model yield similar results to previous studies (Jay et al., 2014; Wendt et al., 2017; Euillades et al., 2017) – a source slightly offset from the eruptive vent and located at ~6 km below the average volcano surface. Although this model provides a good data fit, we do not use it due to several limitations: a) it does not provide an estimate of the source overpressure without assumptions on the source radius, and it cannot explain both well; b) the uplift amplitude NE of the eruptive vent during June-October 2011; and c) the NW-SE signal elongation during the eruption waning in October 2011-February 2012. The CDM model does not provide a satisfactory fit to the RADARSAT-2 interferogram and does not provide the source overpressure, therefore neither this interferogram nor this model are used further (Fig. S5). Instead, we use an horizontal prolate spheroid model which is then used as an input for finite element (FE) spheroids. These FE models can also fit the data by just increasing the spheroid semi-minor axis such that these models allow for calculation of realistic source overpressures within the tensile strength of the rock (\sim 1-40 MPa). These large spheroids violate the boundary conditions of Yang et al. (1988) equations, so they can only be calculated numerically. These horizontal FE spheroids also include the pressure change as a model parameter, allowing it to be coupled with physicochemical simulations. It must be noted that fixing the source geometry makes the physicochemical eruption model developed in the next section geometry dependent and does not allow for proper estimation of the model parameter uncertainties (section S2, Fig. S8).

The inversion predicts a \sim 20 km long spheroid below CC and spanning from CNc to Pv at a depth of \sim 5 km (hereafter M₁), and with its centroid offset \sim 3 km NW from the eruptive vent (Fig. 6). Using a set of models with semi-minor axes between 2 and 3 km

and a shear modulus of 20 GPa, the inverted source pressure drop is \sim 20-50 MPa, within the tensile strength of the rock (section S2), and fits the data with very small residuals (Fig. 6). This spheroid is elongated along the NW-SE direction of the local graben structure, but slightly different from the spheroid reported by Delgado et al. (2016) for the post-eruptive inflation (Table 1). A source radius increase from 2 to 3 km has a negligible effect in the residual of the interferograms that span June-October 2011 but a slight increase in the residual of the October 2011-February 2012 pairs (Figs. 6 and S6-S8). This arises because the data recorded during June-October 2011 are not coherent on top of the volcano, so they are insensitive to the FE spheroid dimensions (Fig. S7). As M₁ cannot fit both the June-October 2011 and October 2011-March 2012 interferograms with residuals of similar amplitude, we invert the latter data independently (Figs. 6, S6-S7). The best fitting inversion for the eruption waning is a slightly deeper spheroid (5.8 vs. 5.2 km for M₁). This second source model (hereafter M₂) is consistent with a slight change in the plumbing system during the eruption waning, in agreement with a second pulse of magma effusion (Coppola et al., 2017b) and with profiles that show that the shape of the deformation signal changed (Fig. S6). Because most of the ground deformation and lava extrusion were recorded during June-October 2011 and the M₁ and M₂ residuals are not statistically significant, we use M₁ in the following sections and hence M₂ is not considered further.

The temporal evolution of the eruption is constrained with a time series of the M_1 FE spheroid pressure drop that will be used in the next sections. This time series is calculated inverting every interferogram for the pressure change and then with a network inversion where the pressure changes are retrieved for every SAR date instead of every interferogram (e.g., Biggs et al., 2010, section S2.2). The time series of pressure drop shows a quasi-exponential pressure drop between -28 and -20 MPa for radii of 2.5 and 3 km respectively (Fig. 7). The maximum subsidence predicted by these

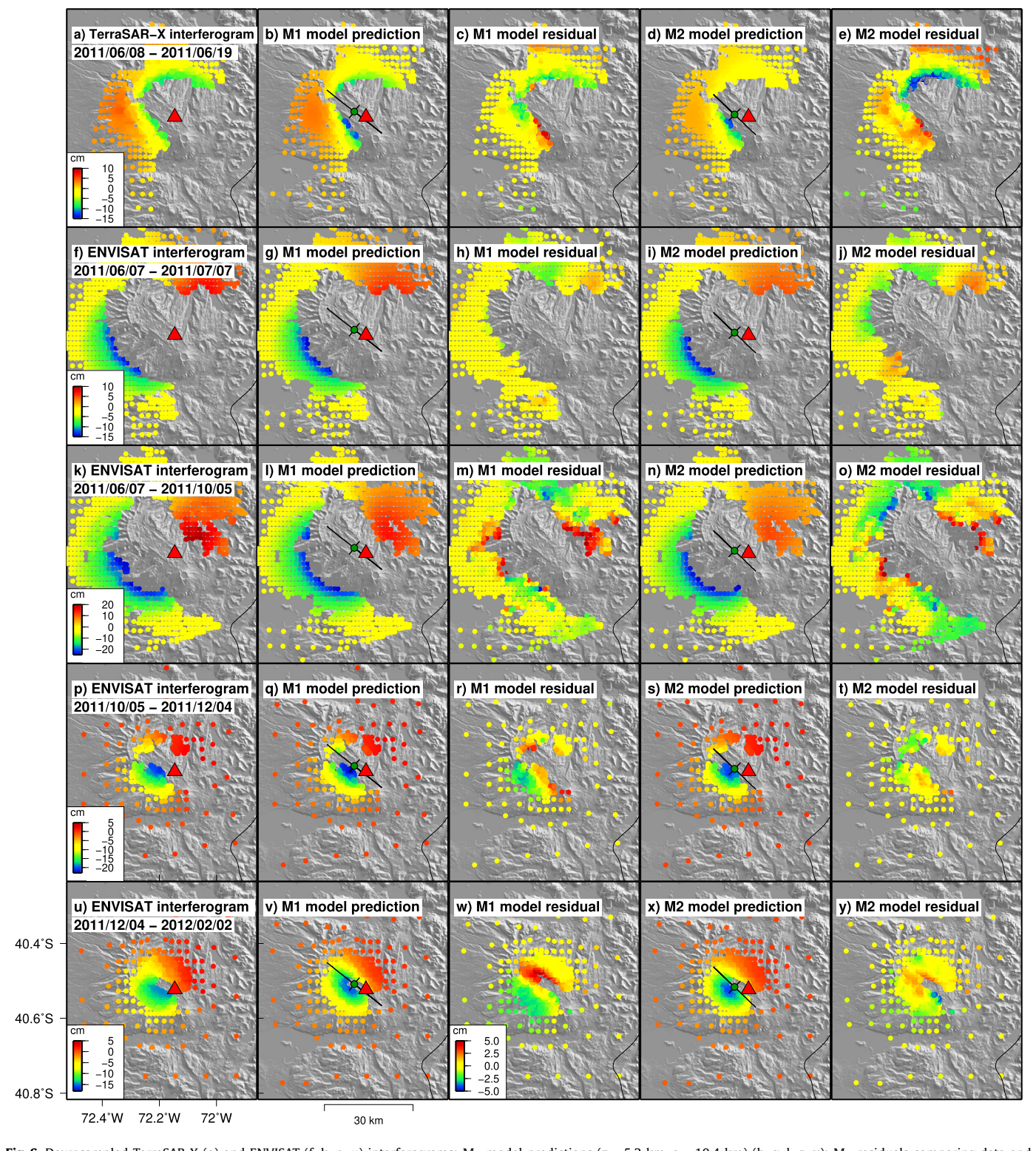


Fig. 6. Downsampled TerraSAR-X (a) and ENVISAT (f, k, p, u) interferograms; M_1 model predictions ($z \sim 5.2$ km, a ~ 10.4 km) (b, g, l, q, v); M_1 residuals comparing data and the model for the inversion of the FE spheroid with a minor semi-axis of 2.5 km (c, h, m, r, w); M_2 model prediction ($z \sim 5.8$ km, a ~ 8.6 km) (d, i, n, s, x); M_2 residuals comparing data and the model for the inversion of the FE spheroid with a minor semi-axis of 2.5 km (e, j, o, t, y). Green circle and black lines show the spheroid centroid and axes. The red triangle is the eruptive vent. The color scales are the same for the interferogram and model predictions in each row and all the residuals have the same color scale. The residual root mean square (RMS) are shown in Fig. S7.

Table 1

Top. Yang spheroid best fit source models. See text for details on the rationale behind M_1 and M_2 models. X_s centroid EW coordinate, Y_s centroid NS coordinate, Z_s centroid depth, a major semi axis, b semi-minor axis. Centroid coordinates are in WGS84 UTM 18S datum. The spheroid plunge and semi-minor axis are fixed to 0 and 1 km. The 2012-2015 spheroid responsible for post-eruptive ground deformation (Delgado et al., 2016) is shown to highlight that the co-eruptive and post-etuptive deformation sources are similar in shape but different in location and depth. For the FE models we increase the M_1 spheroid b to 2.5 and 3 km while keeping the rest of the parameters fixed, resulting in spheroids with volumes of 272 and 392 km³. Bottom: Eruption models best fit source parameters. b FE spheroid semi-minor axis, p_0 initial magma overpressure, c_b conduit conductivity (Equation (4)), β_m magma compressibility, χ_T^w total H_2O content, χ_L^c total CO_2 content. * indicates a fixed parameter. N/A indicates a model parameter that is not calculated by a given model. Note that p_0 is higher for the physicochemical model because the magma density predicted by the model is lower (\sim 2320 kg/m³) than the magma density used in the other models (2200 kg/m³). As the data uncertainties are unrealistically small (see main text), the model parameters uncertainties are very small, hence they are not reported here (Figs. S.11-S12).

Source model	X _s (km)	Y _s (km)	Z _s (km)	a (km)	b (km)	θ	δ
Spheroid M ₁	738.3	5512.0	5.2	10.4	1 (fixed)	0 (fixed)	50
Spheroid M ₂	737.6	5511.1	5.8	8.6	1 (fixed)	0 (fixed)	46
Spheroid 2012-2015	736.6	5513.9	4.6	7.2	1 (fixed)	9	129

Eruption model	b (km)	p ₀ (MPa)	c _b (m ⁴ Pa ⁻¹ s ⁻¹)	β_m (10 ⁻¹⁰ Pa ⁻¹)	χ ^w _{Tot} (% wt)	χ ^c _{Tot} (% ppm)	R (m)	φ (%)	G (GPa)
Exponential	2.5	11	0.043	1.06	N/A	N/A	N/A	N/A	20
Exponential	2.5	-1.3	0.086	2.12	N/A	N/A	N/A	N/A	10
Exponential	3	5.9	0.058	1.05	N/A	N/A	N/A	N/A	20
Lava load	2.5	14.93	0.036	1.05	N/A	N/A	N/A	N/A	20
Lava load	3.0	9.72	0.048	1.04	N/A	N/A	N/A	N/A	20
Physicochemical	2.5	17-19	N/A	1.17	1-3	50*	28-70	50*	20

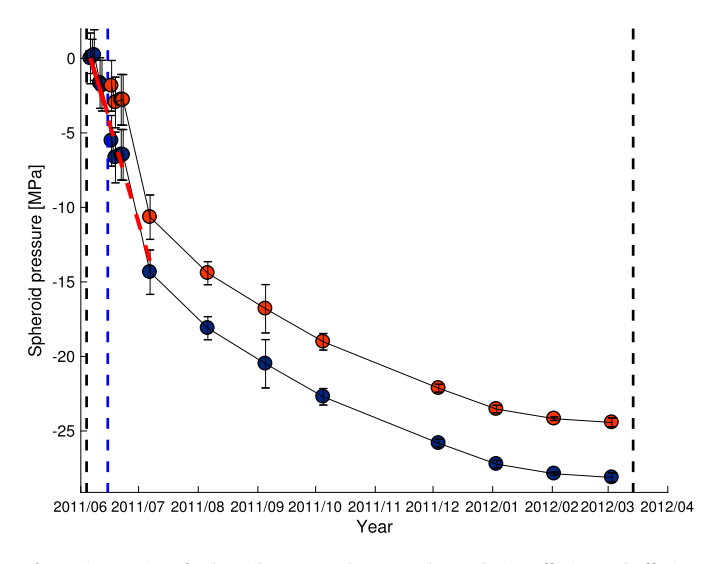


Fig. 7. Time series of spheroid pressure that span the explosive-effusive and effusive phases (blue and red dots respectively) inverted for a source with a semi-minor radius of 2.5 km from the co-eruptive ENVISAT and TSX interferograms. The red dashed and thick lines are the linear pressure drops recorded during the first month of the eruption and during the purely explosive stage. The linear trend during the explosive stage was subtracted from the data to retrieve a time series of pressure drop for the effusive phase only (red points). The vertical black lines are the start and end of the eruption and the vertical blue line is the onset of lava effusion.

best fit FE spheroids varies between 2.2 and 2.5 m between June 7, 2011 and the end of the eruption in March 2012. We note that the source volume cannot be independently resolved from the pressure drop because a larger source implies a smaller pressure drop (Fig. 5 in Anderson and Segall, 2013). Given the lack of sensitivity of the InSAR data to the finite dimensions of the spheroid (Fig. S7), we do not calculate an absolute pressure drop.

3.3. Physicochemical model

The physicochemical model follows the studies of Mastin et al. (2008) and Anderson and Segall (2011). These models simulate the evolution of an effusive eruption and predict time series of both ground deformation and extruded lava volume. The model consists

of a pressurized horizontal prolate spheroid reservoir in a linear elastic half-space under a lithostatic load that contains magma made up of melt, crystals, and exsolved and dissolved volatiles (Liu et al., 2005). The reservoir is connected to the eruptive vent by a conduit, but as the spheroid centroid at CC is clearly offset from the eruptive vent (Fig. 6), for simplicity we assume a dipping conduit. As magma outflows from the reservoir, the flow rate is controlled by the conduit dimensions, reservoir pressure, and magma viscosity, which is a function of the dissolved H2O (Hess and Dingwell, 1996) and the crystal volume fraction (Farguharson et al., 2015). During the eruption, magma piles up on top of the eruptive vent, increasing the lithostatic load on the reservoir, and reducing the pressure gradient that drives the conduit flow. The model is isothermal and does not consider other processes such as variations in magma properties due to decompression in the conduit, conduit degassing, crystal growth, or H₂O exsolution due to magma crystallization (section S4). Therefore magma properties are kept constant as magma ascends in the conduit in all the models used in this study.

We model the time series of extruded volume (Fig. 5) and pressure change inverted from the complete set of interferograms (Fig. 7) with the M₁ spheroid model with semi-minor axes of 2.5 and 3 km, and for the effusive phase only (section S3). The inversions solve for the pressure drop, magma compressibility and conduit conductivity in the exponential and lava load models, and for the total H₂O and CO₂ contents, initial source overpressure and conduit radius in the physicochemical model (model parameter uncertainties in section S4.2). As described earlier, we do not include the reservoir volume as an independent model parameter so we use the reservoir volume derived from the FE models for each time series of pressure drop (Table 1). The most relevant parameters of volcanological interest are the magma compressibility and the total volatile content. The conduit radius and conductivity control the magma flow rate in the conduit, but are of secondary interest for this study compared with the magma volatile phases.

3.3.1. Exponential model with and without lava load

Equations 9-10 (section S4) can be solved analytically for constant magma properties with no recharge (hereafter the exponential model, Anderson and Segall, 2011, 2013).

Table 2 Model parameters used in the exponential eruption model (Equations (1) - (4)).

Parameter	Description	Value
ΔΡ	Reservoir pressure	Modeled
\mathbf{p}_{ch}	Reservoir pressure drop	Inverted
p_{ch_0}	Initial reservoir overpressure	$p_0 + \rho_l g L$
p_0	Magma overpressure	Calculated with p_{ch} and equation (3)
$\overline{\rho_m}$	Depth averaged magma density	2200 kg/m ³
$ ho_{ m l}$	Wall rock density	2700 kg/m ³
ΔV	DRE extruded volume	Modeled
V_0	Spheroid volume	Fixed from kinematic model (Table 1)
β_m	Magma compressibility	Inverted
β_{ch}	Prolate spheroid compressibility	$2\frac{3}{4C}$
G	Shear modulus	10 - 20 GPa
L	Conduit length	Fixed from kinematic model
c_b	Conduit conductivity	Inverted
η	Magma viscosity	not calculated, trade-offs with c_b and R
R	Conduit radius	not calculated, trade-offs with c_b and η

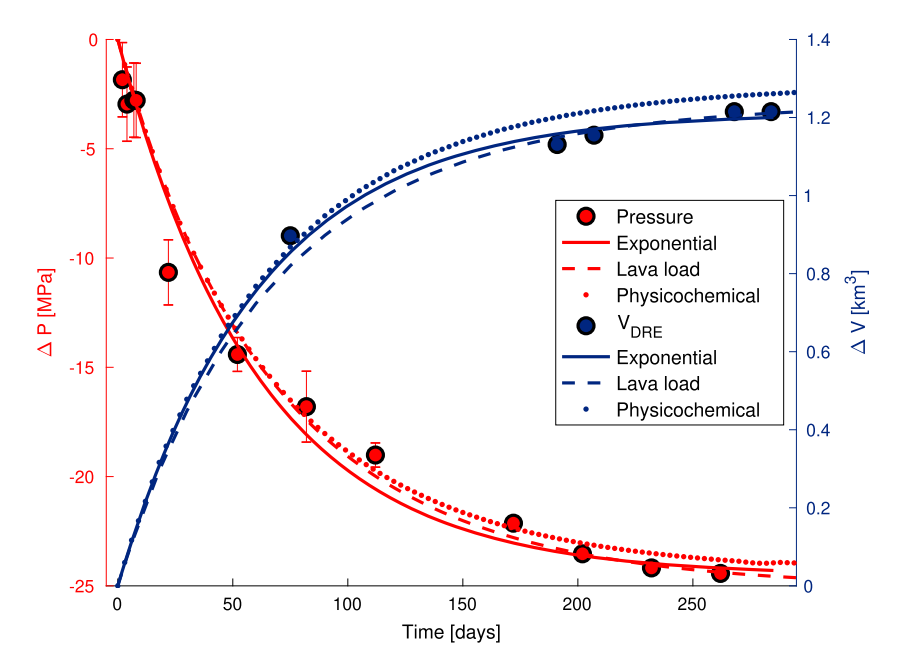


Fig. 8. Joint reservoir pressure and extruded volume time series, with model fits. The red and blue dots are the M_1 pressure drop (ΔP) for a spheroid with a semi-minor axis of 2.5 km and DRE extruded volume time (Δ V) series. The thick lines, dashed lines and points are the synthetic signals predicted by the best fit model parameters from the exponential, lava load and physicochemical eruption models. The error bars of the extruded volume and of the pressure drop during the waning of the eruption are very small, so they are not shown in the figure. The simulation starts at the onset of lava effusion.

$$\Delta P(t) = -p_{ch}(1 - e^{-t/\tau}) \tag{1}$$

$$\Delta V(t) = V_0(\beta_m + \beta_{ch}) p_{ch} (1 - e^{-t/\tau})$$
 (2)

$$p_{ch} = p_{ch_0} - \overline{\rho_m} gL = (\rho_l - \overline{\rho_m}) gL + p_0 \tag{3}$$

$$p_{ch} = p_{ch_0} - \overline{\rho_m} gL = (\rho_l - \overline{\rho_m}) gL + p_0$$

$$\tau = \frac{V_0(\beta_m + \beta_{ch})}{c}, c = \frac{c_b}{L}, c_b = \frac{\pi R^4}{8\eta}$$
(4)

Here equation (1) is the pressure drop in the shallow reservoir, equation (2) is the extruded volume, equation (3) is excess pressure above magmastatic and equation (4) is the exponential time constant as a function of the conduit conductivity c_h (Tables 1, 2 and S2). Despite its simplicity, we use this exponential model in our first set of inversions.

The exponential model predicts the overall temporal evolution of both the reservoir depressurization and the extruded volume, with a magma compressibility of 1.06×10^{-10} Pa⁻¹ (Fig. 8, Table 1). Given the estimates of the magma compressibility, the reservoir volume change ΔV can be calculated with the formula $\Delta V = -V_{ex} \frac{\beta_c}{\beta_c + \beta_m}$ (Anderson and Segall, 2013, page 13). For a shear modulus of 20 GPa and a total erupted volume of 1.21 km³

DRE we calculate $\Delta V \sim -0.5 \text{ km}^3$. Setting the shear modulus from 20 to 10 GPa in the exponential model doubles the conduit conductivity and the magma compressibility, resulting in an unrealistic negative magma overpressure (Table 1). Because this simple model can fit the data well, we do not consider co-eruptive magma recharge in the reservoir in the subsequent simulations. The effect of the lava load on the model changes the force balance in the conduit and requires a numerical solution (hereafter the lava load model, section S4.1). Despite the fact that the inversions predict overpressures ~4 MPa larger than the exponential model to compensate for the increasing load, the inversion results do not change the predicted magma compressibility (Table 1, Fig. 8). The magma compressibilities calculated for semi-minor axes of 2.5 and 3 km are very similar, therefore they are not very sensitive to the spheroid semi-minor axis. In the following calculations we only use time series for the spheroid with a semi-minor axis of 2.5 km.

3.3.2. Physicochemical numerical model

In this model we allow for gas to exsolve in the reservoir due to magma decompression. Then, the gas exsolution changes both the magma compressibility and the viscosity, the latter controlling the conduit flow rate. We find that the only well constrained parameter in this model is the pressure drop with respect to the lithostatic load because inversions with the total CO₂ as a free model parameter show multiple local minima. This model parameter trades-off with the conduit radius and total H₂O, and is dependent on the search scheme in the inversion algorithm. This problem can be partially alleviated by setting the total CO2 content to a small value of 50 ppm, which is justified because the CO₂ is low enough that the rhyolitic magma can be considered as devoid of this gas (see Discussion section). The model predicts a magma overpressure of \sim 17-19 MPa, a conduit radius of 30-70 m, dissolved H₂O of 1-3 wt.% with no exsolved gas phase in the reservoir, a magma compressibility of $\sim 1.17 \times 10^{-10}$ Pa⁻¹ and magma viscosities of 10^6 -10⁸ Pa s. However, the physicochemical model does not provide a significantly better fit to the data than the exponential and the lava load models (Fig. 8, Table 1).

4. Discussion

4.1. Lava flow extrusion and shallow laccolith intrusion

Significant topographic changes with amplitudes of \sim 250 m are observed E of the eruptive vent area in the January-August 2011 dDEM (Fig. 4) and interpreted by Castro et al. (2016) as being produced by the emplacement of a shallow laccolith at depths < 400 m during the first month of eruption. The DRE volume of the laccolith and the lava flow is \sim 1.45 km³, similar to the 1.3 km³ bulk of Castro et al. (2016), while the bulk volume of the lava flow from MODIS imagery is \sim 0.6 km³, equivalent to \sim 0.54 km³ DRE. The difference of these two numbers is \sim 0.91 km³ DRE for the shallow laccolith, higher than the bulk \sim 0.8 km³ reported by Castro et al. (2016) (section S1.2.4). Our lava flow thicknesses are in agreement with our own visual observations in January 2017 on the N side of the flow (\sim 30 m), and similar to those calculated by Castro et al. (2016) (Fig. 1), but 4 times larger than the 35 m assumed by Bertin et al. (2015) and Tuffen et al. (2013) because measurements from its edges are not representative of its actual thickness. The shallow laccolith emplacement also produced a distributed uplift signal to the SE of the eruptive vent (Fig. S3) as well as a clear post-emplacement topographic decrease of \sim 40 m in the area of the laccolith itself (Fig. 4c, e), but they are not described in this study. Castro et al. (2016) proposed that the flow thickness is \sim 50 m and most of the \sim 150 m of topographic change in the flow itself was produced by the shallow laccolith intrusion. If this would be true, there should be a higher topographic change closer to the eruptive vent and in the middle of the lava flow, but this is not the case because the flow thicknesses are similar W, S and N of the eruptive vent and only abruptly decrease at its edges

Castro et al. (2016) argued that the shallow laccolith was emplaced during the first month of the eruption, during both the explosive and effusive stages based on morphological analysis of TSX amplitude images around the eruptive vent, and due to a reduction in the conduit radius that increased the overpressure in the conduit. Radar amplitude images that complement the analysis of Castro et al. (2016) show that significant morphological changes occurred during the explosive stage of the eruption. Indeed, there were clear topographic changes in the area of the eruptive vent as of June 6, 2011 (Figs. 3 and S4). This implies that a non-negligible fraction of the laccolith was emplaced before the onset of lava extrusion and coeval with magma fragmentation, and at depths similar to those predicted by magma fragmentation models (Castro et al., 2016). The mechanism responsible for this apparent paradox is beyond the scope of this study.

4.2. Volcano plumbing system source models: correlation with two pulses of lava discharge

The spheroid source M_1 located beneath Cordón Caulle that fits the data during the effusive phase is elongated along the NW-SE direction from CNc to Pv, and implies a large plumbing system located beneath these three edifices at shallow depths ($z \sim 5$ km). This likely implies lateral magma transfer during the whole eruption and not only during the first three eruption days (Jay et al., 2014). Nevertheless, this interpretation could be biased by the lack of InSAR data on top of the volcano during most of the eruption. It also implies that the eruption was likely tectonically controlled, as suggested for the long term volcano evolution (Lara et al., 2006), for the post-eruptive inflation (Delgado et al., 2016) and indirectly shown for the eruption by Wendt et al. (2017). The deformation source active during the effusive phase is slightly different than the one active during the 2012-2015 post-eruptive uplift (Delgado et al., 2016, Table 1).

There is clear evidence during the effusive phase for a slight change in the deformation source in October-December 2011 (Fig. 2, Figs. S6-S7), an increase in the TADR when it reached \sim 15 m³/s in October 2011 (Coppola et al., 2017b; Bertin et al., 2015), and an increase in the quasi-harmonic tremor during October -November 2011 (Bertin et al., 2015). These changes are interpreted as due to a second pulse of lava extrusion during the waning of the effusive stage (Fig. 5). The second extrusion pulse is not observed in the dDEM nor in the GPS data of Wendt et al. (2017) because of the poor spatio-temporal sampling of these data sets. The spheroid that can explain the deformation data during this second pulse between October 2011 and March 2012 (M₂) is slightly deeper than M₁, but it is also located within the large plumbing system because it is not statistically different than the M_1 model (Fig. S7). Renewed lava effusion pulses during eruption waning have also been observed during the 2008-2009 Chaiten rhyolitic eruption (Pallister et al., 2013) and at several basaltic systems (Bonny and Wright, 2017). It is possible that the pressure drop between June and October 2011 was large enough to remobilize magma from interconnected reservoirs at similar depths, but not to trigger additional intrusions from a deeper source, which likely happened right after the end of the eruption resulting in \sim 77 cm of post-eruptive uplift (Delgado et al., 2016). The latter might require a much larger pressure gradient achievable only when the TADR reached its minimum at the end of the eruption. We speculate that magma from a different part of the large crystal mush that likely underlies the volcano was remobilized during the second effusive pulse. Future petrological studies should consider this hypothesis.

4.3. Comparison between exponential and physicochemical eruption models

Although both the exponential and physicochemical models can fit the data reasonably well, there are some differences in the model predictions (Fig. 8). The main difference arises in the fit to the time series of extruded volume, as the physicochemical model predicts a slightly higher magma volume for a compressibility of $\sim 1.17 \times 10^{-10} \text{ Pa}^{-1}$ with 1-3.0 wt.% of H₂O in the reservoir, whereas the exponential model predicts a magma compressibility of $\sim 1.06 \times 10^{-10}$ Pa s. Given the data uncertainties, the magma compressibilities predicted by the exponential, lava load and physicochemical models are basically the same. Regardless of the type of model, these compressibilities are half the 2.1 $(\pm 0.4) \times 10^{-10}$ Pa s calculated by Jay et al. (2014) for the explosive phase and are only attainable if the magma in the reservoir had little or no exsolved volatiles (following paragraphs), hence magma compressibility variations are only produced by pressure changes in the melt and crystal fractions. It is possible to improve the fit of the extruded volume data if the melt and crystal compressibilities are reduced, although thermodynamical modeling precludes smaller values (Table S2). Wendt et al. (2017) suggested that there is a missing volume required to account for the mismatch between the volume change of the deflating source and the lava flow volume during the onset of the effusive phase and this is indeed due to the large volume of the shallow laccolith.

Uncertainties in the shear modulus also have an effect in the estimated magma compressibility. Halving this modulus doubles the estimated magma compressibility (Table 1), to values similar to those estimated by Jay et al. (2014) for the explosive phase, which is unrealistic for the onset of lava effusion. We speculate that the slightly poorer fit of the physicochemical model to the time series of extrusion volume is due to the removal of some of the lava flow volume when accounting for the volume of the laccolith intruded during the explosive phase. This results in a slightly lower compressibility in the exponential model inversion that is not possible to reach in the physicochemical model. On the other hand, differences between the models and the data can be explained by the eruption being made of two pulses of lava extrusion rather than one (Coppola et al., 2017b), although this is not possible to constrain with the poor temporal sampling of both the InSAR and dDEM data. The slight differences in the temporal evolution predicted by the exponential and physicochemical models can also be explained by the time constant. In the exponential model, the flow rate is controlled by the conduit conductivity, a function of the conduit radius, length, and magma viscosity, whereas in the physicochemical model these parameters are decoupled, as the viscosity is a function of the dissolved H₂O content. This implies that the conduit conductivity that controls the flow rate changes between the different models because it depends on a different set of model parameters.

The volatile contents of the CC rhyolite erupted in the explosive stage of the eruption are \sim 4 wt.% H₂O and 220 ppm CO₂ (Jay et al., 2014) and 0.44-1.23 wt.% H₂O and 38-71 ppm CO₂ (Castro et al., 2013), but the only estimate in the scientific literature for the effusive phase at the time of writing (April 2019) is from Tuffen et al. (2013) who reported glass H_2O contents ≤ 0.2 wt.% but no CO_2 measurements. The dissolved water content $\chi_{H_2O_d}$ of a rhyolitic magma in the upper crust can be approximated by Henry's law for a CO₂-free magma and is given by $\chi_{H_2O_d} = 4.1 \times 10^{-6} \sqrt{P}$ with P the pressure in Pa (Jaupart and Tait, 1990). This simple formula predicts very similar dissolved H₂O for a CO₂-free magma at pressures < 200 MPa than the solubility model used in the physicochemical model (Liu et al., 2005). Magma stored at a depth of 5.2 km in a crust with a density of 2700 kg/m³ may dissolve up to 4.8 wt.% of H₂O, which is considerably higher than the range of 1-3 wt.% predicted by the physicochemical model. These calculations imply that the magma in the reservoir at the onset of the lava effusion was already degassed with respect to its equilibrium condition, due to the violent decompression during the explosive phase. However, the measured dissolved water in the lava flow is much lower, < 0.2 wt.% (Tuffen et al., 2013), which implies a variety of gas loss mechanisms. These include a) volatiles were lost as magma ascended in the conduit (Eichelberger, 1995), b) volatiles remained in the magma leading to magma fragmentation in the upper conduit resulting in hybrid lava extrusion coeval to explosive Vulcanian blasts (Schipper et al., 2013), and c) some volatiles were lost through flow in the permeable conduit (Jaupart and Allegre, 1991). These mechanisms are discussed elsewhere (Schipper et al., 2013; Castro et al., 2014). The range of predicted viscosities (10⁶ - 10⁸ Pa s) are also higher compared to those calculated for the explosive phase of 10^4 - 10^5 Pa s (Castro et al., 2013).

Observations of the conduit geometry are also scarce. A visual overflight on June 20, 2011, reported an elliptical conduit of 50×100 m (Castro et al., 2013). These dimensions are within the

range of model predictions of \sim 30-70 m for the conduit radius (Table 1), which must be considered as an average during the eruption. Deviations from an exponential function in the time series of extruded volume are evidence for changes in the conduit radius (Stasiuk et al., 1993; Castruccio et al., 2017), but these are not observed during the effusive phase so the conduit conductivity remained constant during the effusive phase.

In summary, both models do a reasonable job of approximating the evolution of the eruption with a wide conduit, and magma compressibilities of $\sim\!1.1\times10^{-10}~Pa^{-1}$ in a partially degassed rhyolitic reservoir, much lower than 2.5-5 x $10^{-10}~Pa^{-1}$ for the dacitic dome of the 2004-2008 eruption of Mt St. Helens (Mastin et al., 2009). The compressibility of the rhyolitic lava are due to changes in the crystal and liquid phases, not in the gas phase. Finally, these models do not consider inelastic effects such as conduit clogging that might end the eruptions earlier than the model predictions, as observed during the Bardarbunga eruption (Gudmundsson et al., 2016; Coppola et al., 2017a), and the fact that a pure exponential predicts that the eruption will never end.

4.4. Limitations on satellite observations needed for constraining physicochemical eruption models

Despite the key results obtained by the combination of InSAR and physicochemical eruption models, there are several limitations that preclude the systematic use of this type of models. A geometry-independent inversion for an spheroid of arbitrary dimensions and coupled with magma physics and conduit flow is computationally intensive and time consuming. Further, due to the poor temporal sampling of the dDEM data, the time series of extruded volume is aliased, and as described earlier, this could also bias the inverted model parameters. On the other hand, if the goal is to forecast the temporal evolution of an eruption that shows an exponential trend using data with poor temporal sampling, there is no real gain using a fully numerical model because the predicted time series are very similar for both models. The key difference is that the physicochemical model can decouple the compressibility resulting from gas exsolution from the melt and crystal compressibilities. Clearly the pressure drop inverted from the exponential model can be biased because it does not consider the effect of the surface load that counterbalances the pressure gradient that drives the conduit flow. However, this effect can be neglected if the flow thicknesses are < 40 m (Fig. S10).

Aside from this study, only (Anderson and Poland, 2016) have used InSAR and dDEM data in physicochemical models of magma supply, storage and eruption rates. In contrast, their study at Kilauea Volcano used a steady-state model rather than a timedependent simulation. Advances in these eruption models applied to effusive eruptions require time series of extruded volume with a much better temporal resolution than those currently achievable from either airborne LIDAR or photogrammetry (\sim 1 week to \sim 1 month) (e.g., Schilling et al., 2008) and from the TanDEM-X mission (11 days). This is highlighted by the difference in elevation in two of the dDEMs in the shallow laccolith (Fig. 4g, i) due to potential post-emplacement processes. To our knowledge, the only exception is the airborne NASA GLISTIN Ka-band interferometer that recorded five DEMs during the first month of the 2018 Kilauea eruption (NASA Disasters Program, 2018). As the TanDEM-X mission was designed to create a global DEM rather than tracking time-lapse topographic changes on the Earth's surface (Rizzoli et al., 2017), its repeat period is not optimal for studying lava flow extrusion. Only Cordón Caulle, Tolbachik (Kubanek et al., 2017) and Bardarbunga (Dirscherl and Rossi, 2018) volcanoes have dDEM time series of lava extrusion that show either exponential or logarithmic trends, and these are biased by the TDX poor temporal sampling (e.g., Poland, 2014).

The DEM temporal sampling is more problematic for optical data such as Pléiades (Nakada et al., 2017) and WorldView (Dai and Howat, 2017) because these images are also limited by cloud coverage, a systematic problem at many volcanoes. On the other hand, there are many stereo optical satellites, and if their observations could be coordinated over erupting volcanoes, better time series could be possible. Currently, high temporal resolution (1 image per 1-3 days) TADR can only be achieved from high-temporal, but low-spatial resolution (\sim 1 km/pixel) systems such as MODIS thermal imagery by means of an energy balance, but their reliability is a matter of debate (Dragoni and Tallarico, 2009; Ganci et al., 2018). Given the low frequency of these long-lasting effusive eruptions, future improvements in this type of models will likely rely on DEMs acquired by drones and better use of the constellation of high-resolution optical satellites and TanDEM-X.

5. Conclusions

A unique data set of SAR observations including ground deformation interferometry, radar amplitude and DEMs provide an unprecedented view of the effusive phase of the 2011-2012 Cordón Caulle eruption. Further, a physicochemical eruption model constrained with these data sets provides insights into the temporal evolution of the eruption and the volatile budget of the extruded rhyolitic flow. This is the first time that these sets have been available during a rhyolitic eruption, and that these models have been constrained using satellite data only. InSAR data recorded 2.2 - 2.5 m of co-eruptive deflation throughout the eruption effusive phase, produced by deflation of a shallow spheroid at a depth of \sim 5 km. The spheroid location and geometry slightly changed in October 2011, interpreted to be related to a second pulse of lava extrusion. DEMs and radar amplitude images constrain both the extrusion of the lava flow and the intrusion of a very shallow laccolith, the latter inferred to have occurred during both the explosive and effusive stages of the eruption. The lava flow and laccolith maximum topographic change are \sim 150 and 250 m respectively, with a combined joint volume of \sim 1.45 km 3 DRE. A physicochemical eruption model predicts both the quasi-exponential reservoir deflation trend and total extruded volume, and that the reservoir total H2O was halfway between a degassed rhyolite and a gas rich reservoir, with no exsolved gases in the reservoir. Additional gas loss occurs in the conduit, in agreement with visual observations of hybrid lava effusion and explosive activity.

Despite the good spatial coverage of InSAR data, the low number of SAR acquisitions and systematic decorrelation produced by tephra deposition precludes a more detailed assessment of the reservoir geometry, potential changes and temporal evolution. Complex eruptive sequences require a very high temporal sampling rate to discriminate between multiple sources of deformation and their temporal evolution. Future advances in physicochemical models constrained with InSAR data would benefit from TanDEM-X or other DEMs acquired at a much higher temporal sampling rate than the currently available — at best once every 11 days, but in practice they are less frequent.

Acknowledgements

F.D. and M.P were partially supported by NASA's Science Mission Directorate grant NNX16AK87G and NSF grant EAR-1824160. F.D. acknowledges CONICYT PFCHA/DOCTORADO BECAS CHILE/2012-72130089 for a PhD scholarship, NASA for the Earth and Space Sciences Fellowships 16-EARTH16F-0211 and 17-EARTH17R-0058, Jet Propulsion Laboratory (JPL) for the SURP fellowship SP.17.0003.007, and Centre National d'Etudes Spatiales (CNES, France) for a postdoctoral scholarship. Part of this study was carried out at JPL and the U.S. Geological Survey (USGS) Volcano

Science Center during a research visit of F.D. to these institutions. Any use of trade, firm, or product names is for descriptive purposes only and does not imply endorsement by the U.S. Government. This is the U.S. Geological survey publication 1750. ENVISAT raw images were provided by the European Space Agency (ESA) and Level 1 processed single look complex images are freely available at the ESA Online Dissemination site. TerraSAR-X and RADARSAT-2 data were provided by Deutsches Zentrum für Luft- und Raumfahrt (DLR) and the Canadian Space Agency (CSA) and MacDonald. Dettwiler & Associates (MDA) Ltd. respectively through the scientific quota available to the CEOS Latin America Volcano Pilot Project coordinated by Michael Poland (USGS) and Simona Zoffoli (Agenzia Spatiale Italiana). TanDEM-X DEMs and CoSSC data were provided by DLR through the DEM proposals #DEM_GEOL2437 and NTI_INSA0405. The Pléiades data are copyright property of Airbus DS, were provided through the CNES ISIS program under an academic license for the research project 16-0219-01-011-114 and are not available for open distribution. We thank Jennifer Jay for providing the processed ENVISAT interferograms used in her study of the 2011-2012 eruption (Jay et al., 2014); Daniel Bertin (Red Nacional de Vigilancia Volcanica SERNAGEOMIN, now at University of Auckland) for providing the picture shown in Fig. 1 and the lava flow outlines; Diego Coppola (Università di Torino) for the MODIS-derived extrusion data shown in Fig. 5; Christopher Siron (Cornell University) and Whyjay Zheng (Cornell University) for their help with the ArcGIS and Ames Stereo Pipeline softwares respectively; Arthur Delorme (IPGP) for his help with the Mic-Mac software, Raphaël Grandin (IPGP), Tara Shreve (IPGP), Michael Poland (USGS) and Michael Clynne (USGS) for their comments. We also acknowledge two anonymous reviewers and Editor Rajdeep Dasgupta for their comments that significantly improved the quality of this manuscript. Several figures were created with the GMT software (Wessel and Smith, 1998). The processed data sets and intermediate products are available upon request to the authors.

Appendix A. Supplementary material

Supplementary material related to this article can be found online at https://doi.org/10.1016/j.epsl.2019.115736.

References

Anderson, K., Segall, P., 2011. Physics-based models of ground deformation and extrusion rate at effusively erupting volcanoes. J. Geophys. Res., Solid Earth 116. https://doi.org/10.1029/2010jb007939.

Anderson, K., Segall, P., 2013. Bayesian inversion of data from effusive volcanic eruptions using physics-based models: application to Mount St. Helens 2004-2008.
J. Geophys. Res., Solid Earth 118 (5), 2017–2037. https://doi.org/10.1002/jgrb. 50169.

Anderson, K.R., Poland, M.P., 2016. Bayesian estimation of magma supply, storage, and eruption rates using a multiphysical volcano model: Kīlauea Volcano, 2000–2012. Earth Planet. Sci. Lett. 447, 161–171. https://doi.org/10.1016/j.epsl. 2016.04.029.

Bertin, D., Lara, L.E., Basualto, D., Amigo, Á., Cardona, C., Franco, L., Gil, F., Lazo, J., 2015. High effusion rates of the Cordón Caulle 2011–2012 eruption (Southern Andes) and their relation with the quasi-harmonic tremor. Geophys. Res. Lett. 42 (17), 7054–7063. https://doi.org/10.1002/2015GL064624.

Biggs, J., Lu, Z., Fournier, T., Freymueller, J.T., 2010. Magma flux at Okmok Volcano, Alaska, from a joint inversion of continuous GPS, campaign GPS, and interferometric synthetic aperture radar. J. Geophys. Res., Solid Earth 115. https:// doi.org/10.1029/2010jb007577.

Bonadonna, C., Pistolesi, M., Cioni, R., Degruyter, W., Elissondo, M., Baumann, V., 2015. Dynamics of wind-affected volcanic plumes: the example of the 2011 Cordón Caulle eruption, Chile. J. Geophys. Res., Solid Earth 120 (4), 2242–2261. https://doi.org/10.1002/2014/B011478.

Bonny, E., Wright, R., 2017. Predicting the end of lava flow-forming eruptions from space. Bull. Volcanol. 79 (7). https://doi.org/10.1007/s00445-017-1134-8.

Castro, J.M., Schipper, C.I., Mueller, S.P., Militzer, A.S., Amigo, A., Parejas, C.S., Jacob, D., 2013. Storage and eruption of near-liquidus rhyolite magma at Cordon Caulle, Chile. Bull. Volcanol. 75 (4), 17. https://doi.org/10.1007/s00445-013-0702-9.

- Castro, J.M., Bindeman, I.N., Tuffen, H., Schipper, C.I., 2014. Explosive origin of silicic lava: textural and delta D-H2O evidence for pyroclastic degassing during rhyolite effusion. Earth Planet. Sci. Lett. 405, 52–61. https://doi.org/10.1016/j.epsl. 2014.08.012
- Castro, J.M., Cordonnier, B., Schipper, C.I., Tuffen, H., Baumann, T.S., Feisel, Y., 2016. Rapid laccolith intrusion driven by explosive volcanic eruption. Nat. Commun. 7. https://doi.org/10.1038/ncomms13585.
- Castruccio, A., Diez, M., Gho, R., 2017. The influence of plumbing system structure on volcano dimensions and topography. J. Geophys. Res., Solid Earth. https:// doi.org/10.1002/2017IB014855.
- Coppola, D., Ripepe, M., Laiolo, M., Cigolini, C., 2017a. Modelling satellite-derived magma discharge to explain caldera collapse. Geology 45 (6), 523–526. https:// doi.org/10.1130/g38866.1.
- Coppola, D., Laiolo, M., Franchi, A., Massimetti, F., Cigolini, C., Lara, L.E., 2017b. Measuring effusion rates of obsidian lava flows by means of satellite thermal data. J. Volcanol. Geotherm. Res. https://doi.org/10.1016/j.jvolgeores.2017.09.003.
- Dai, C.L., Howat, I.M., 2017. Measuring lava flows with ArcticDEM: application to the 2012-2013 eruption of Tolbachik, Kamchatka. Geophys. Res. Lett. 44 (24), 12133-12140. https://doi.org/10.1002/2017g1075920.
- Delgado, F., Pritchard, M.E., Basualto, D., Lazo, J., Cordova, L., Lara, L.E., 2016. Rapid reinflation following the 2011-2012 rhyodacite eruption at Cordon Caulle volcano (Southern Andes) imaged by InSAR: evidence for magma reservoir refill. Geophys. Res. Lett. 43 (18), 9552-9562. https://doi.org/10.1002/2016gl070066.
- Dirscherl, M., Rossi, C., 2018. Geomorphometric analysis of the 2014–2015 Bárðarbunga volcanic eruption, Iceland. Remote Sens. Environ. 204, 244–259. https://doi.org/10.1016/J.RSE.2017.10.027.
- Dragoni, M., Tallarico, A., 2009. Assumptions in the evaluation of lava effusion rates from heat radiation. Geophys. Res. Lett. 36. https://doi.org/10.1029/2009gl037411.
- Dumont, S., Sigmundsson, F., Parks, M.M., Drouin, V.J.P., Pedersen, G.B.M., Jónsdóttir, I., Höskuldsson, Á., Hooper, A., Spaans, K., Bagnardi, M., Gudmundsson, M.T., Barsotti, S., Jónsdóttir, K., Högnadóttir, T., Magnússon, E., Hjartardóttir, Á.R., Dürig, T., Rossi, C., Oddsson, B., 2018. Integration of SAR data into monitoring of the 2014–2015 Holuhraun eruption, Iceland: contribution of the Icelandic volcanoes supersite and the FutureVolc projects. Front. Earth Sci. 6, 231. https://doi.org/10.3389/feart.2018.00231.
- Eichelberger, J.C., 1995. Silicic volcanism: ascent of viscous magmas from crustal reservoirs. Annu. Rev. Earth Planet. Sci. 23, 41–63. https://doi.org/10.1146/ annurev.ea.23.050195.000353.
- Euillades, P.A., Euillades, L.D., Blanco, M.H., Velez, M.L., Grosse, P., Sosa, G.J., 2017. Co-eruptive subsidence and post-eruptive uplift associated with the 2011–2012 eruption of Puyehue-Cordón Caulle, Chile, revealed by DlnSAR. J. Volcanol. Geotherm. Res. https://doi.org/10.1016/j.jvolgeores.2017.06.023.
- Farquharson, J.I., James, M.R., Tuffen, H., 2015. Examining rhyolite lava flow dynamics through photo-based 3D reconstructions of the 2011-2012 lava flow-field at Cordon-Caulle, Chile. J. Volcanol. Geotherm. Res. 304, 336–348. https://doi.org/10.1016/j.jvolgeores.2015.09.004.
- Ganci, G., Cappello, A., Bilotta, G., Herault, A., Zago, V., Del Negro, C., 2018. Mapping volcanic deposits of the 2011–2015 Etna eruptive events using satellite remote sensing. Front. Earth Sci. https://doi.org/10.3389/feart.2018.00083.
- Gudmundsson, M.T., Jonsdottir, K., Hooper, A., Holohan, E.P., Halldorsson, S.A., Ofeigsson, B.G., Cesca, S., Vogfjord, K.S., Sigmundsson, F., Hognadottir, T., Einarsson, P., Sigmarsson, O., Jarosch, A.H., Jonasson, K., Magnusson, E., Hreinasdottir, S., Bagnardi, M., Parks, M.M., Hjorleifsdottir, V., Palsson, F., Walter, T.R., Schopfer, M.P.J., Heimann, S., Reynolds, H.I., Dumont, S., Bali, E., Gudfinnsson, G.H., Dahm, T., Roberts, M.J., Hensch, M., Belart, J.M.C., Spaans, K., Jakobsson, S., Gudmundsson, G.B., Fridriksdottir, H.M., Drouin, V., Durig, T., Adalgeirsdottir, G., Riishuus, M.S., Pedersen, G.B.M., van Boeckel, T., Oddsson, B., Pfeffer, M.A., Barsotti, S., Bergsson, B., Donovan, A., Burton, M.R., Aiuppa, A., 2016. Gradual caldera collapse at Bardarbunga volcano, Iceland, regulated by lateral magma outflow. Science 353 (6296), 262. https://doi.org/10.1126/science.aaf8988.
- Hess, K.U., Dingwell, D.B., 1996. Viscosities of hydrous leucogranitic melts: a non-Arrhenian model. Am. Mineral. 81 (9–10), 1297–1300.
- Hreinsdottir, S., Sigmundsson, F., Roberts, M.J., Bjornsson, H., Grapenthin, R., Arason, P., Arnadottir, T., Holmjarn, J., Geirsson, H., Bennett, R.A., Gudmundsson, M.T., Oddsson, B., Ofeigsson, B.G., Villemin, T., Jonsson, T., Sturkell, E., Hoskuldsson, A., Larsen, G., Thordarson, T., Oladottir, B.A., 2014. Volcanic plume height correlated with magma-pressure change at Grimsvotn Volcano, Iceland. Nat. Geosci. 7 (3), 214–218. https://doi.org/10.1038/ngeo2044.
- Huppert, H.E., Woods, A.W., 2002. The role of volatiles in magma chamber dynamics. Nature 420 (6915), 493–495. https://doi.org/10.1038/nature01211.
- Jaupart, C., Allegre, C.J., 1991. Gas content, eruption rate and instabilities of eruption regime in silicic volcanoes. Earth Planet. Sci. Lett. 102 (3-4), 413-429. https:// doi.org/10.1016/0012-821x(91)90032-d.
- Jaupart, C., Tait, S., 1990. Dynamics of eruptive phenomena. Rev. Miner. 24, 213–238.
- Jay, J., Costa, F., Pritchard, M., Lara, L., Singer, B., Herrin, J., 2014. Locating magma reservoirs using InSAR and petrology before and during the 2011-2012 Cordon Caulle silicic eruption. Earth Planet. Sci. Lett. 403, 463. https://doi.org/10.1016/j. epsl.2014.07.021.

- Kubanek, J., Westerhaus, M., Heck, B., 2017. TanDEM-X time series analysis reveals lava flow volume and effusion rates of the 2012–2013 Tolbachik, Kamchatka fissure eruption. J. Geophys. Res., Solid Earth. https://doi.org/10.1002/2017/B014309.
- Lara, L.E., Naranjo, J.A., Moreno, H., 2004. Rhyodacitic fissure eruption in Southern Andes (Cordon Caulle, 40.5 degrees S) after the 1960 (Mw: 9.5) Chilean earthquake: a structural interpretation. J. Volcanol. Geotherm. Res. 138 (1–2), 127–138. https://doi.org/10.1016/j.jvolgeores.2004.06.009.
- Lara, L.E., Lavenu, A., Cembrano, J., Rodriguez, C., 2006. Structural controls of volcanism in transversal chains: Resheared faults and neotectonics in the Cordon Caulle-Puyehue area (40.5 degrees S), Southern Andes. J. Volcanol. Geotherm. Res. 158 (1–2), 70–86. https://doi.org/10.1016/j.jvolgeores.2006.04.017.
- Liu, Y., Zhang, Y.X., Behrens, H., 2005. Solubility of H20 in rhyolitic melts at low pressures and a new empirical model for mixed H20-CO2 solubility in rhyolitic melts. J. Volcanol. Geotherm. Res. 143 (1-3), 219-235. https://doi.org/10.1016/j. jvolgeores.2004.09.019.
- Lohman, R.B., Simons, M., 2005. Some thoughts on the use of InSAR data to constrain models of surface deformation: noise structure and data downsampling. Geochem. Geophys. Geosyst. 6, 12. https://doi.org/10.1029/2004gc000841.
- Mastin, L.G., Roeloffs, E., Beeler, N.M., Quick, J.E., 2008. Constraints on the size, overpressure, and volatile content of the Mount St. Helens magma system from geodetic and dome-growth measurements during the 2004–2006+ eruption. In: Sherrod, D.R., Scott, W.E., Stauffer, P.H. (Eds.), A Volcano Rekindled, the Renewed Eruption of Mount St. Helens, 2004–2006. In: U.S. Geological Survey Professional Paper, vol. 1750, p. 856.
- Mastin, L.G., Lisowski, M., Roeloffs, E., Beeler, N., 2009. Improved constraints on the estimated size and volatile content of the Mount St. Helens magma system from the 2004-2008 history of dome growth and deformation. Geophys. Res. Lett. 36. https://doi.org/10.1029/2009gl039863.
- McTigue, D.F., 1987. Elastic stress and deformation near a finite spherical magma body: resolution of the point source paradox. J. Geophys. Res., Solid Earth 92 (B12), 12931–12940. https://doi.org/10.1029/JB092iB12p12931.
- Nakada, S., Zaennudin, A., Yoshimoto, M., Maeno, F., Suzuki, Y., Hokanishi, N., Sasaki, H., Iguchi, M., Ohkura, T., Gunawan, H., Triastuty, H., 2017. Growth process of the lava dome/flow complex at Sinabung Volcano during 2013–2016. J. Volcanol. Geotherm. Res. https://doi.org/10.1016/j.jvolgeores.2017.06.012.
- Neal, C.A., Brantley, S., Antolik, L., Babb, J., Burgess, M., Calles, K., Cappos, M., Chang, J.C., Conway, S., Desmither, L., Dotray, P., Elias, T., Fukunaga, P., Fuke, S., Johanson, I.A., Kamibayashi, K., Kauahikaua, J., Lee, R.L., Pekalib, S., Miklius, A., Million, W., Moniz, C.J., Nadeau, P.A., Okubo, P., Parcheta, C., Patrick, M.P., Shiro, B., Swanson, D.A., Tollett, W., Trusdell, F., Younger, E.F., Zoeller, M.H., Montgomery-Brown, E.K., Anderson, K.R., Poland, M.P., Ball, J., Bard, J., Coombs, M., Dietterich, H.R., Kern, C., Thelen, W.A., Cervelli, P.F., Orr, T., Houghton, B.F., Gansecki, C., Hazlett, R., Lundgren, P., Diefenbach, A.K., Lerner, A.H., Waite, G., Kelly, P., Clor, L., Werner, C., Mulliken, K., Fisher, G., 2018. The 2018 rift eruption and summit collapse of Kīlauea Volcano. Science 363 (6425), 367–374. https://doi.org/10.1126/science.aav7046.
- Nikkhoo, M., Walter, T.R., Lundgren, P.R., Prats-Iraola, P., 2016. Compound dislocation models (CDMs) for volcano deformation analyses. Geophys. J. Int. https://doi.org/ 10.1093/gji/ggw427.
- Pallister, J.S., Diefenbach, A.K., Burton, W.C., Munoz, J., Griswold, J.P., Lara, L.E., Lowenstern, J.B., Valenzuela, C.E., 2013. The Chaiten rhyolite lava dome: eruption sequence, lava dome volumes, rapid effusion rates and source of the rhyolite magma. Andean Geol. 40 (2), 277–294. https://doi.org/10.5027/andgeoV40n2a06.
- Pistolesi, M., Cioni, R., Bonadonna, C., Elissondo, M., Baumann, V., Bertagnini, A., Chiari, L., Gonzales, R., Rosi, M., Francalanci, L., 2015. Complex dynamics of small-moderate volcanic events: the example of the 2011 rhyolitic Cordon Caulle eruption, Chile. Bull. Volcanol. 77 (1). https://doi.org/10.1007/s00445-014-0898-3.
- Poland, M.P., 2014. Time-averaged discharge rate of subaerial lava at Kilauea Volcano, Hawai'i, measured from TanDEM-X interferometry: implications for magma supply and storage during 2011-2013. J. Geophys. Res., Solid Earth 119 (7), 5464–5481. https://doi.org/10.1002/2014jb011132.
- Reath, K., Pritchard, M., Poland, M., Delgado, F., Carn, S., Coppola, D., Andrews, B., Ebmeier, S.K., Rumpf, E., Henderson, S., Baker, S., Lundgren, P., Wright, R., Biggs, J., Lopez, T., Wauthier, C., Moruzzi, S., Alcott, A., Wessels, R., Griswold, J., Ogburn, S., Loughlin, S., Meyer, F., Vaughan, G., Bagnardi, M., 2019. Thermal, deformation, and degassing remote sensing time series (CE 2000-2017) at the 47 most active volcanoes in Latin America: implications for volcanic systems. J. Geophys. Res., Solid Earth. https://doi.org/10.1029/2018/B016199.
- Rivalta, E., Segall, P., 2008. Magma compressibility and the missing source for some dike intrusions. Geophys. Res. Lett. 35 (4). https://doi.org/10.1029/ 2007gl032521.
- Rizzoli, P., Martone, M., Gonzalez, C., Wecklich, C., Tridon, D.B., Brautigam, B., Bachmann, M., Schulze, D., Fritz, T., Huber, M., Wessel, B., Krieger, G., Zink, M., Moreira, A., 2017. Generation and performance assessment of the global TanDEM-X digital elevation model. ISPRS J. Photogramm. Remote Sens. 132, 119–139. https://doi.org/10.1016/j.isprsjprs.2017.08.008.

- Sambridge, M., 1999. Geophysical inversion with a neighbourhood algorithm I. Searching a parameter space. Geophys. J. Int. 138 (2), 479–494. https://doi.org/10.1046/j.1365-246X.1999.00876.x.
- Schilling, S.P., Thompson, R.A., Messerich, J.A., Iwatsubo, E.Y., 2008. Use of digital aerophotogrammetry to determine rates of lava dome growth, mount St. Helens, Washington, 2004–2005. In: Sherrod, D.R., Scott, W.E., Stauffer, P.H. (Eds.), A Volcano Rekindled, the Renewed Eruption of Mount St. Helens, 2004–2006. U.S. Geological Survey Professional Paper, pp. 145–167.
- Schipper, C.I., Castro, J.M., Tuffen, H., James, M.R., How, P., 2013. Shallow vent architecture during hybrid explosive-effusive activity at Cordon Caulle (Chile, 2011-12): evidence from direct observations and pyroclast textures. J. Volcanol. Geotherm. Res. 262, 25–37. https://doi.org/10.1016/j.jvolgeores.2013.06.005.
- Schipper, C.I., Castro, J.M., Tuffen, H., Wadsworth, F.B., Chappell, D., Pantoja, A.E., Simpson, M.P., Le Ru, E.C., 2015. Cristobalite in the 2011-2012 Cordon Caulle eruption (Chile). Bull. Volcanol. 77 (5). https://doi.org/10.1007/s00445-015-0925-7.
- Segall, P., 2013. Volcano deformation and eruption forecasting. Remote Sens. Volcan. Volcan. Process.: Integrat. Observ. Model. 380, 85–106. https://doi.org/10.1144/sp380.4.
- Smittarello, D., Cayol, V., Pinel, V., Peltier, A., Froger, J.L., Ferrazzini, V., 2019. Magma propagation at Piton de la Fournaise from joint inversion of InSAR and GNSS. J. Geophys. Res., Solid Earth. https://doi.org/10.1029/2018JB016856.
- Sparks, R.S.J., 2003. Forecasting volcanic eruptions. Earth Planet. Sci. Lett. 210 (1–2), 1–15. https://doi.org/10.1016/s0012-821x(03)00124-9.

- Sparks, R.S.J., Biggs, J., Neuberg, J.W., 2012. Monitoring volcanoes. Science 335 (6074), 1310–1311. https://doi.org/10.1126/science.1219485.
- Stasiuk, M.V., Jaupart, C., Sparks, R.S.J., 1993. On the variations of flow-rate in nonexplosive lava eruptions. Earth Planet. Sci. Lett. 114 (4), 505–516. https://doi.org/10.1016/0012-821x(93)90079-o.
- Tuffen, H., James, M.R., Castro, J.M., Schipper, C.I., 2013. Exceptional mobility of an advancing rhyolitic obsidian flow at Cordon Caulle volcano in Chile. Nat. Commun. 4, 7. https://doi.org/10.1038/ncomms3709.
- Wendt, A., Tassara, A., Baez, J.C., Basualto, D., Lara, L.E., García, F., 2017. Possible structural control on the 2011 eruption of Puyehue-Cordon Caulle volcanic complex (southern Chile) determined by InSAR, GPS and seismicity. Geophys. J. Int. 208 (1), 134–147. https://doi.org/10.1093/gji/ggw355.
- Wessel, P., Smith, W.H.F., 1998. New, improved version of generic mapping tools released. Eos, Trans. Am. Geophys. Union 79 (47), 579. https://doi.org/10.1029/98F000426
- Xu, W.B., Jonsson, S., Ruch, J., Aoki, Y., 2016. The 2015 Wolf volcano (Galapagos) eruption studied using Sentinel-1 and ALOS-2 data. Geophys. Res. Lett. 43 (18), 9573–9580. https://doi.org/10.1002/2016gl069820.
- Yang, X.M., Davis, P.M., Dieterich, J.H., 1988. Deformation from inflation of a dipping finite prolate spheroid in an elastic half-space as a model for volcanic stressing. J. Geophys. Res. B, Solid Earth Planets 93 (5), 4249–4257. https://doi.org/10.1029/JB093iB05p04249.